

Article

Petrography and Organic Geochemistry Characterizations of Lower Paleozoic Organic-Rich Shale in the Northwestern Upper Yangtze Plate: Niutitang Formation and Longmaxi Formation, Dabashan Foreland Belt

Delu Li ^{1,*}, Rongxi Li ², Di Zhao ¹ and Feng Xu ³

¹ College of Geology and Environment, Xi'an University of Science and Technology, Xi'an 710054, China; zhaodi95@foxmail.com

² School of Earth Sciences and Resources, Chang'an University, Xi'an 710054, China; rongxi99@163.com

³ Shaanxi Center of Geological Survey, Xi'an 710068, China; 2018027004@chd.edu.cn

* Correspondence: lidelu322@126.com

Received: 22 August 2018; Accepted: 25 September 2018; Published: 9 October 2018



Abstract: Measurements of total organic carbon, Rock-Eval pyrolysis, X-ray diffraction, scanning electron microscope, maceral examination, gas chromatography, and gas chromatography-mass spectrometry were conducted on the organic-rich shale of Lower Paleozoic Niutitang Formation and Longmaxi Formation in Dabashan foreland belt to discuss the organic matter characteristic, organic matter origin, redox condition, and salinity. The results indicate that the Niutitang Formation and Longmaxi Formation organic-rich shale are good and very good source rocks with Type I kerogen. Both of the shales have reached mature stage for generating gas. Biomarker analyses indicate that the organic matter origin of Niutitang Formation and Longmaxi Formation organic-rich shale are all derived from the lower bacteria and algae, and the organic matter are all suffered different biodegradation degrees. During Niutitang Formation and Longmaxi Formation period, the redox conditions are both anoxic with no stratification and the sedimentary water is normal marine water.

Keywords: petrography; organic geochemistry; organic-rich shale; Niutitang Formation; Longmaxi Formation; Dabashan foreland belt

1. Introduction

China has vast shale gas exploration prospects. Up to 2012, the Chinese shale gas geological reserves have reached $134 \times 10^{12} \text{ m}^3$ with $25 \times 10^{12} \text{ m}^3$ recoverable resources [1]. However, due to the differences in exploration degree, the main proven area of shale gas exploration focused on south China, especially Sichuan Basin [2–5]. Massive studies indicate that the northern Sichuan Basin, Dabashan belt, develops numerous organic-rich shale formations [6–10]. The significant formations are mainly Niutitang Formation and Longmaxi Formation of Lower Paleozoic. The deposition thicknesses of these two formations are relatively large [11–15], and are affected by later tectonic movement, their burial depth is rather shallow, displaying good prospect of shale gas exploration [16,17]. Whereas, the current research of both formations have primarily focused on tectonic evolution history, element geochemistry, and organic matter enrichment [18–24]. Their petrography and organic geochemistry characterizations were poorly researched. In this contribution, four profiles were measured, and each of the two of them were Niutitang Formation and Longmaxi Formation. Based on total organic carbon (TOC), Rock-Eval pyrolysis, X-ray diffraction, scanning electron microscope, maceral examination, gas chromatography, and gas chromatography-mass spectrometry, their petrography and organic

geochemistry characteristics will be discussed. The first aim of the study is to provide a comprehensive description of the geochemical characteristics of organic-rich shale from the Lower Paleozoic Niutitang Formation and Longmaxi Formation. The second aim is to characterize their organic matter origin, redox, and salinity environment.

2. Geological Setting

Located between Yangtze block and Qinling orogenic belt, Dabashan belt is divided into three secondary tectonic belts: Dabashan thrust nappe belt; Dabashan foreland belt; and Dabashan foreland depression [25] (Figure 1). Since the Sinian Period, the Dabashan foreland belt mainly underwent two periods (marine carbonate platform and foreland lacustrine basin) [26]. In Cambrian, Dabashan foreland belt were epeiric sea environment and developed neritic facies [6,27–30]. Till the late Silurian, affected by Caledonian movement, the Dabashan foreland belt uplifted comprehensively and stayed in a long-term rising state [27–30]. This orogeny movement lasts for 120 million years and leads to the absence of Upper Silurian–Carboniferous stratum [27–30]. Later, a massive transgression event happened in Late Carboniferous—Early Permian [27–30]. In Middle-Late Triassic, Indosinian movement caused the collision of the North China Plate and the South China Plate, resulting in the fold uplift in Dabashan foreland belt [27–30]. After the Late Cretaceous, the plate underwent extensional tectonics [31,32]. In the Lower Paleozoic, the Upper Yangtze Plate was a marine sedimentary facies and the Dabashan foreland belt developed into a deep water shelf environment [33]. The main organic-rich shale in the Lower Paleozoic develops in Niutitang Formation (ϵ_{1-2n}) and Longmaxi Formation (O_3S_{1l}).

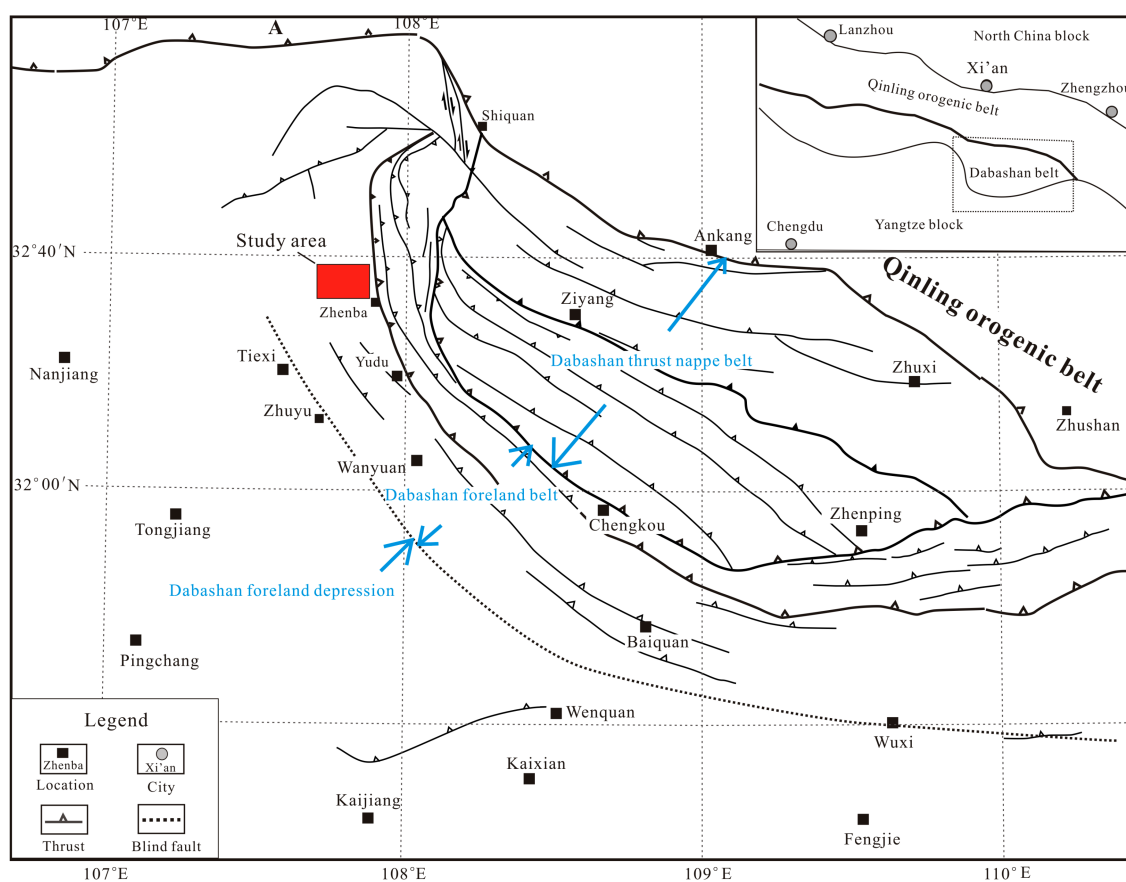


Figure 1. Tectonic setting map of the Dabashan belt in the northwestern Upper Yangtze Plate (modified from [31]).

The Dabashan foreland belt develops the strata of Ediacaran to Jurassic. The Lower Paleozoic develops Cambrian, Ordovician, and Silurian stratum. Niutitang Formation is at the basal of Cambrian, and Longmaxi Formation is at the uppermost of Ordovician and the basal of Silurian. Both formations have the integrated contact relationship with the upper and the lower strata. The thickness of Niutitang Formation is almost 120 m with siliceous shale, carbonaceous shale, shale, and silty mudstone. While, Longmaxi Formation mainly develops siliceous shale (graptolite fossil), carbonaceous shale, and mudstone with almost 20 m thickness (Figure 2).

3. Sampling and Methods

Ten siliceous shale samples were obtained from Niutitang Formation and Longmaxi Formation in the Dabashan foreland belt. Each formation was measured with two sections. The sections' positions, rock assemblages, and sampling locations are shown in Figure 2. All samples were collected in Kraft bags till they were used in experiments with minimal contamination and oxidation. Ten samples were measured for total organic carbon (TOC), Rock-Eval pyrolysis, X-ray diffraction (XRD), scanning electron microscope (SEM), and maceral examination. On four samples, gas chromatography (GC) and gas chromatography-mass spectrometry (GC-MS) were performed.

For TOC, analysis samples were crushed to powder under 200 meshes and the inorganic carbon was removed by diluted hydrochloric acid. After being combusted at 1200 °C in oxygen flow, organic carbon could be transformed to CO₂ using a Multi EA2000 (Analytik Jena AG, Thuringia, Germany). The samples were analyzed in the LECO CS-400 analyzer (LECO Corporation, St. Joseph, MI, USA).

For Rock-Eval pyrolysis, the instrument was first warmed-up. Then pyrolysis analysis was conducted on powder samples using Rock-Eval equipment (LECO Corporation, Chicago, IL, USA). Samples of mass 30 mg were heated to 600 °C in a helium atmosphere and S₁, S₂, S₃, S₄, and T_{max} were measured.

For mineral content analysis, XRD was performed with a D8 ADVANCE powder diffractometer with Cu K α radiation from 5° to 60°, a step increment of 0.02°, and a counting time of two seconds per step. The minerals were identified from the diffractograms by referencing to the ICDD Powder Diffraction File. The analytical uncertainty is less than 1% precision.

SEM was conducted in Hitachi S-4800 (Hitachi High-Technologies Corporation, Tokyo, Japan). The electronic image resolution is 3.5 nm (30 KV), and the sensitivity is 0.1 Z with the 0.5–30 kV acceleration voltage. Amplification factor is in range of $\times 20$ – $\times 500$.

For maceral examination, oil immersion lenses were used with an optical microscope fitted with a microphotometer, to measure vitrinite reflectance. The samples were crushed and sieved through 20 mesh and dissolved using HCl and HF. The dry fractions were polished. The percentage compositions of macerals were counted in the eyepiece cross hairs with an area of (0.1 mm \times 0.2 mm). Reflectance values were used to generate a histogram, and vitrinite reflectance could be confirmed by standard data under 20 °C and 35% humidity.

GC and GC-MS analyses were conducted on a SHIMADZU GC-2010 (SHIMADZU, Kyoto, Japan), equipped with a 30 m \times 0.25 mm \times 0.25 mm HP-5 fused silica capillary column, and an Agilent 6890GC/5975i MS (Agilent Technologies Inc., Santa Clara, CA, USA) with a 60 m \times 0.25 mm \times 0.25 mm HP-5MS fused silica capillary column, respectively. He is the carrier gas. The gas was boosted at a rate of 1.0 mL/min. The mass spectrometer was conducted in the electron ionization mode, and the data of the saturated fraction, terpane, and sterane were acquired.

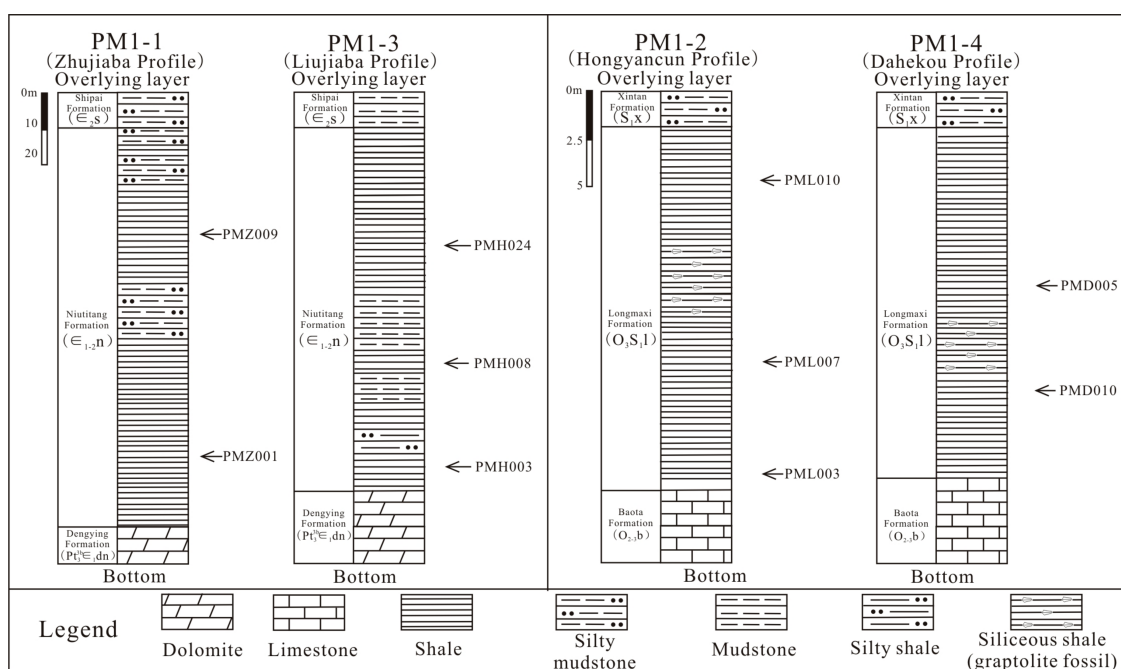


Figure 2. The sampling locations of Niutitang Formation and Longmaxi Formation.

4. Results

4.1. Mineralogical Characteristics

The results of XRD analysis are listed in Table 1. Quartz dominates in samples of both in Niutitang Formation and Longmaxi Formation, with an average concentration of 49.92 wt % (45.50–55.80 wt %) and 50.74 wt % (41.00–59.50 wt %). Illite takes the second largest portion with the average of 30.78 wt % (24.4–39.50 wt %) and 34.48 wt % (33.10–35.30 wt %). Besides, chlorite, plagioclase, K-feldspar, pyrite, dolomite, and calcite are all in a small portion. In Niutitang Formation, pyrite mould hole can be seen in the coexistence with organic matter (Figure 3A). Affected by oxidation, some pyrite obviously went through limonitization (Figure 3B). Some corrosion holes in feldspar can also be observed and are beneficial to hydrocarbon occurrence (Figure 3C). In Longmaxi Formation, pyrite framboids with the particle diameter of less than 1 μm exist mostly with organic matter (Figure 3D). Illite is mostly in the form of thin sheet (Figure 3E), and calcite has obvious fracture (Figure 3F).

Table 1. The mineral content of the shale samples.

Minerals (wt %)	Niutitang Formation						Longmaxi Formation					
	PMZ001	PMZ009	PMH003	PMH008	PMH024	Avg.	PMD005	PMD010	PML003	PML007	PML010	Avg.
Quartz	45.50	53.80	55.80	47.70	46.80	49.92	41.00	46.30	59.50	58.90	48.00	50.74
Illite	24.40	32.40	21.90	39.50	35.70	30.78	35.30	34.90	34.40	33.10	34.70	34.48
Chlorite	0.00	0.30	0.00	0.00	0.00	0.06	6.80	5.10	0.00	0.00	3.70	3.12
Plagioclase	25.40	13.50	19.80	12.80	17.50	17.80	11.90	5.80	6.10	8.00	13.60	9.08
K-feldspar	4.70	0.00	2.50	0.00	0.00	1.44	0.00	0.00	0.00	0.00	0.00	0.00
Pyrite	0.00	0.00	0.00	0.00	0.00	0.00	5.00	2.50	0.00	0.00	0.00	1.50
Dolomite	0.00	0.00	0.00	0.00	0.00	0.00	0.00	5.10	0.00	0.00	0.00	1.02
Calcite	0.00	0.00	0.00	0.00	0.00	0.00	0.00	0.30	0.00	0.00	0.00	0.06

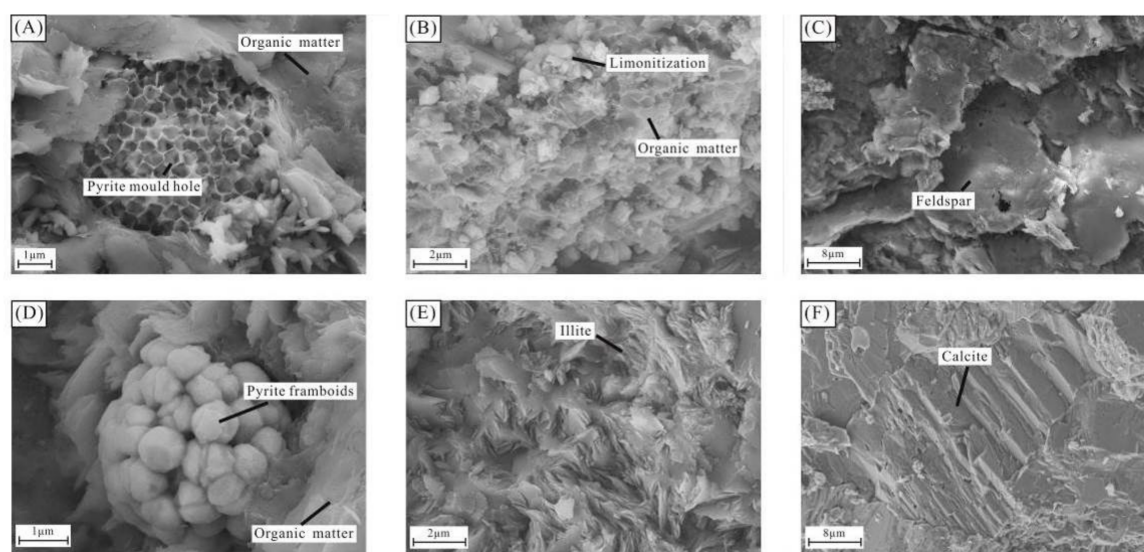


Figure 3. SEM of minerals characteristics. (A) PMZ001; (B) PMH008; (C) PMH024; (D) PMD010; (E) PML003; and (F) PML007. (A–C) Niutitang Formation; and (D–F) Longmaxi Formation.

4.2. Organic Petrography

The results of maceral examination are listed in Table 2. Sapropelinite takes the most portions in both Niutitang Formation and Longmaxi Formation. Besides, a small number of vitrinite-like and inertinite are also detected (Table 2). The amorphous can be perceived under microscope in both formations, and the solid bitumen is normally associated with pyrite (Figure 4).

Table 2. The microscopic constituents of organic matter of the shale samples.

Formation	Sample ID	Sapropelinite (%)	Exinite (%)	Vitrinite-Like (%)	Inertinite (%)	TI
Niutitang Formation	PMZ001	98.00	0	1.41	0.59	96.35
	PMH003	96.25	0	2.81	0.94	93.20
	PMH008	96.00	0	2.40	1.60	92.60
Longmaxi Formation	PMD005	96.48	0	1.87	1.65	93.42
	PMD010	97.18	0	0.80	2.01	94.57
	PML003	92.95	0	2.54	4.51	86.53

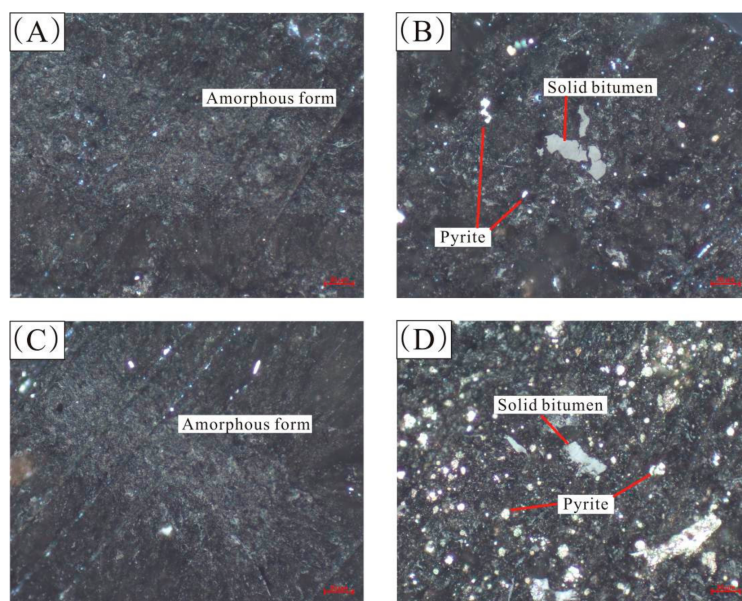


Figure 4. Photos of maceral examination. (A) PMZ001; (B) PMH008; (C) PMD005; and (D) PML003. (A,B) Niutitang Formation; and (C,D) Longmaxi Formation.

4.3. TOC and Rock-Eval

The results of TOC and Rock-Eval are listed in Table 3. The TOC of siliceous shale samples of Niutitang Formation and Longmaxi Formation ranges from 1.15 wt % to 3.66 wt %, and from 3.14 wt % to 4.42 wt % (Table 3). T_{max} of the samples of Niutitang Formation and Longmaxi Formation ranges in 486–511 °C and 517–580 °C, respectively. S_2 of the samples of both formations is very low with the range of 0.03–0.08 mg/g and 0.03–0.06 mg/g (Table 3). High T_{max} with low S_2 is probably caused by relatively high maturity. Additionally, the potential yield ($S_1 + S_2$) of the samples also shows very low value with the range of 0.10–11 and 0.10–0.13 mg/g (Table 3). S_3 and S_4 of the samples of Niutitang Formation are in the range of 1.60–2.267 mg/g and 14.61–66.67 mg/g, while S_3 and S_4 of Longmaxi Formation are in the range of 1.35–1.78 mg/g and 13.52–31.39 mg/g (Table 3). Furthermore, HI of Niutitang Formation and Longmaxi Formation vary in the range of 0.9–5.29 mg/g TOC and 0.96–2.40 mg/g TOC (Table 3). OI of Niutitang Formation and Longmaxi Formation vary in the range 40.01–151.31 mg/g TOC and 42.95–132.81 mg/g TOC (Table 3).

4.4. N-Alkanes Characteristic and Isoprenoid

Saturated hydrocarbon chromatogram of Niutitang Formation and Longmaxi Formation both show almost bimodal type with relatively wide range of main peak (Figure 5). The peak assignments are listed in Appendix A. The main peak of shale samples of Niutitang Formation are C_{24} and C_{18} . The carbon preference index (CPI) is 1.23 and 1.45 with the odd-even predominance of 1.06 and 1.03 (Table 4). The C_{21+}/C_{22+} is 0.21 and 1.05 and $(nC_{21} + nC_{22})/(nC_{28} + nC_{29})$ is 1.69 and 2.36 (Table 4). Pr/nC_{17} and Ph/nC_{18} of the samples are 0.59 and 0.57, and 0.74 and 0.75. The Pr/Ph is 0.58 and 0.76, respectively (Table 4). The main peak of shale samples of Longmaxi Formation are C_{17} and C_{18} (Table 4). The carbon preference index (CPI) is 1.24 and 1.26 with the odd-even predominance of 1.04 and 0.93 (Table 4). The C_{21+}/C_{22+} is 0.73 and 1.00 and $(nC_{21} + nC_{22})/(nC_{28} + nC_{29})$ is 2.57 and 1.58. Pr/nC_{17} and Ph/nC_{18} of the samples are 0.66 and 0.58, and 0.82 and 0.85 (Table 4). The Pr/Ph is 0.7 and 0.8 (Table 4). As can be seen, the samples of Niutitang Formation and Longmaxi Formation all show no odd-carbon number predominance (Figure 5). N-alkanes without odd-carbon number predominance normally reflect two organic matter origin types [34,35]. One stems from bacteria and other microbial wax, and the other comes from high plant wax remolded by bacteria [34,35]. In Cambrian and Silurian, the higher plants did not appear. Thus, high carbon number does not indicate the source of parent

material of terrestrial higher plants. Considering the biodegradation of N-alkanes (especially under C₂₁), the samples of Niutitang Formation and Longmaxi Formation all underwent different degrees of biodegradation.

Table 3. Results of TOC and pyrolysis data of samples from Niutitang Formation and Longmaxi Formation.

Formations	Samples ID	TOC (wt %)	T _{max} (°C)	S ₂ (mg/g)	S ₁ + S ₂ (mg/g)	S ₃ (mg/g)	S ₄ (mg/g)	HI (mg/g TOC)	OI (mg/g TOC)
Niutitang Formation	PMZ001	1.62	493	0.08	0.11	1.96	15.06	5.29	129.5
	PMZ009	1.78	511	0.05	0.10	2.25	14.82	3.36	151.31
	PMH003	3.66	511	0.03	0.10	2.21	28.4	2.11	77.64
	PMH008	1.74	510	0.08	0.11	1.6	14.61	3.41	109.08
	PMH024	1.15	486	0.03	0.10	2.67	66.67	0.9	40.01
Longmaxi Formation	PMD005	3.14	517	0.06	0.10	1.38	28.79	1.04	47.88
	PMD010	3.21	578	0.05	0.11	1.35	31.39	1.27	42.95
	PML003	4.42	541	0.06	0.10	1.8	13.52	2.21	132.81
	PML007	3.97	577	0.03	0.13	1.66	33.2	2.4	49.89
	PML010	3.45	580	0.04	0.10	1.78	31.33	0.96	56.75

TOC: Total organic carbon. T_{max}: maximum peak temperature of Rock-Eval pyrolysis S₂. S₁: Volatile hydrocarbon content. S₂: Remaining HC generative potential. S₁ + S₂: Potential of generating hydrocarbon. S₃: CO₂ content. S₄: 10 × residual organic carbon. HI: Hydrogen Index = S₂ × 100/TOC. OI: Oxygen Index = S₃ × 100/TOC.

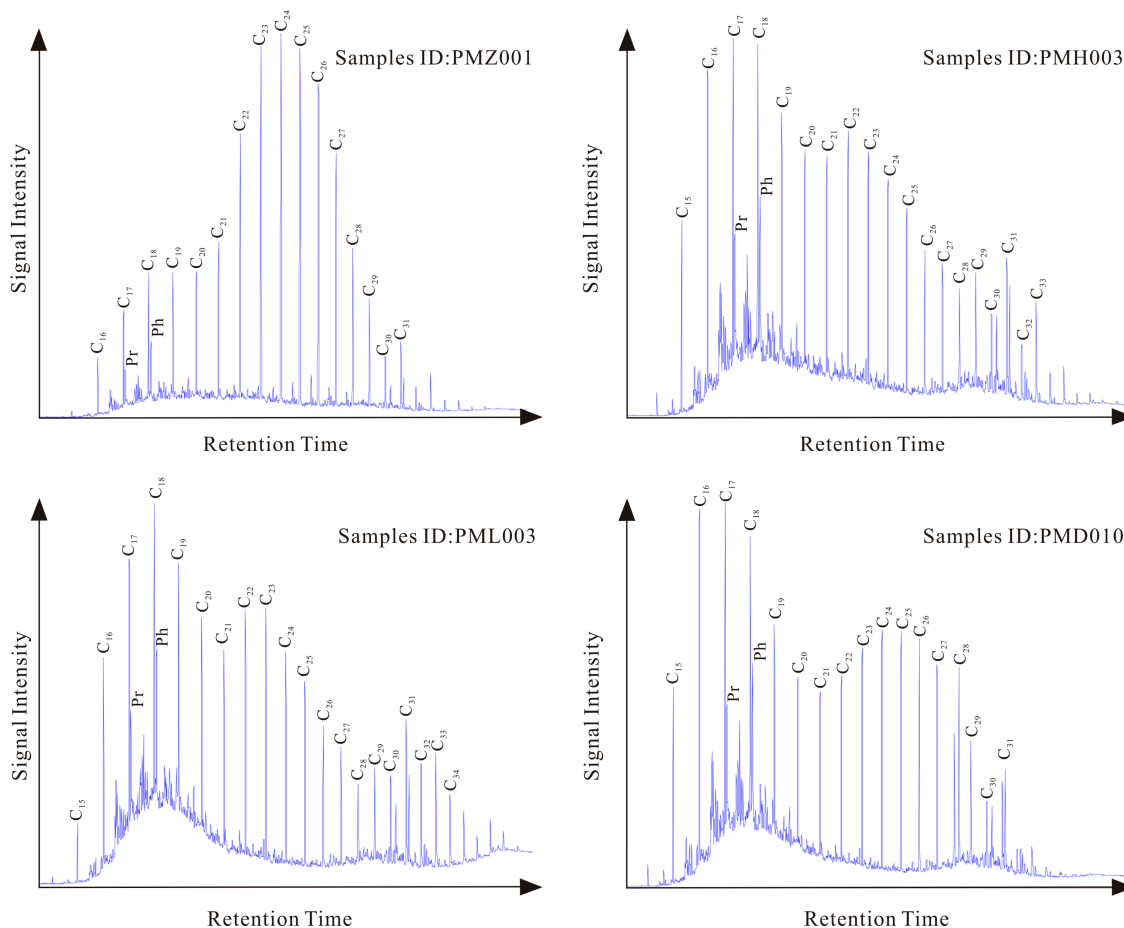


Figure 5. M/z85 mass fragment grams of saturated hydrocarbon fractions.

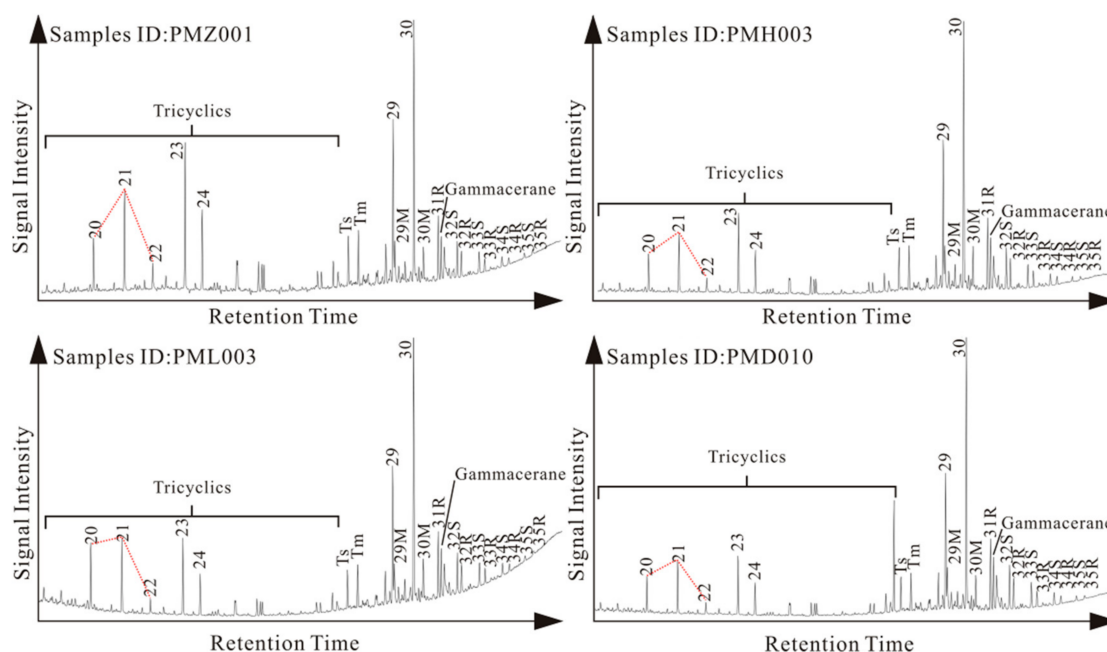
Table 4. Parameters of n-alkanes and isoprenoid.

Formations	Samples ID	CPI	OEP	C ₂₁₊ /C ₂₂₊	(nC ₂₁ + nC ₂₂)/(nC ₂₈ + nC ₂₉)	Pr/nC ₁₇	Ph/nC ₁₈	Pr/Ph	Peak Number
Niutitang Formation	PMZ001	1.23	1.06	0.21	1.69	0.59	0.74	0.58	C ₂₄
	PMH003	1.45	1.03	1.05	2.36	0.57	0.75	0.76	C ₁₈
Longmaxi Formation	PML003	1.24	1.04	0.73	2.57	0.66	0.82	0.7	C ₁₈
	PMD010	1.26	0.93	1.00	1.58	0.58	0.85	0.8	C ₁₇

Note: OEP: odd-even predominance = $(C_{23} + 6 \times C_{25} + C_{27}) / (4 \times C_{24} + 4 \times C_{26})$; 8; CPI: carbon preference index = $[(C_{25} + C_{27} + C_{29} + C_{31} + C_{33}) / (C_{24} + C_{26} + C_{28} + C_{30} + C_{32}) + (C_{25} + C_{27} + C_{29} + C_{31} + C_{33}) / (C_{26} + C_{28} + C_{30} + C_{32} + C_{34})] / 2$.

4.5. Terpenes

The shale samples of Niutitang Formation and Longmaxi Formation are detected with high abundant of tricyclic terpene (Figure 6). Normally, tricyclic terpene stem from algae and bacteria, and its thermal stability is stronger than pentacyclic triterpene, especially for C₁₉–C₄₅ of tricyclic terpene [36–38]. As discussed before, the samples of Niutitang Formation and Longmaxi Formation suffered biodegradation. That is the reason why the samples contain high tricyclic terpene content.

**Figure 6.** M/z191 mass fragment grams of saturated hydrocarbon fractions.

The Ts/(Ts + Tm) of the samples of Niutitang Formation is 0.49, with 0.95 and 0.98 of Ts/Tm, respectively (Table 5). The C₃₁22S/(22S + 22R) and C₂₁/C₂₃ tricyclic terpene are 0.59 and 0.57, and 0.71 and 0.79. The C₂₆/C₂₅ tricyclic terpene is 0.99 and 0.95 (Table 5). The Ts/(Ts + Tm) of the samples of Longmaxi Formation is 0.57 and 0.58, with 0.95 and 0.97 of Ts/Tm, respectively (Table 5). The C₃₁22S/(22S + 22R) and C₂₁/C₂₃ tricyclic terpene are 0.59 and 0.57, and 0.96 and 0.87. The C₂₆/C₂₅ tricyclic terpene is 0.92 and 0.98 (Table 5).

In saturated hydrocarbon fractions of the samples, hopane compounds are also detected with the most high abundance of C₃₀ hopane. The $\beta\alpha$ -moretane/ $\alpha\beta$ -hopane of the samples of Niutitang Formation is 0.14 and 0.17, While the $\beta\alpha$ -moretane/ $\alpha\beta$ -hopane of Longmaxi Formation is 0.17 and 0.14 (Table 5). Moreover, low concentrations of gammacerane has been detected with the gammacerane/ $\alpha\beta$ C₃₀ hopane of 0.17 and 0.14 in Niutitang Formation and Longmaxi Formation, respectively (Table 5). Additional relevant parameters are shown in Table 5.

Table 5. Parameters of terpanes and steranes.

Formations	Samples ID	1	2	3	4	5	6	7	8	9	10	11	12	13	14	15	16	17		
																		C ₂₇	C ₂₈	C ₂₉
Niutitang Formation	PMZ001	0.49	0.95	0.59	0.59	0.51	0.44	0.14	0.17	0.24	7.33	0.17	0.77	0.71	0.99	1.45	0.40	35.33	30.82	33.86
	PMH003	0.49	0.98	0.57	0.58	0.44	0.43	0.17	0.17	0.27	5.87	0.17	0.71	0.79	0.95	0.95	1.00	31.52	31.73	36.74
Longmaxi Formation	PML003	0.49	0.95	0.57	0.60	0.44	0.46	0.17	0.14	0.28	5.78	0.14	0.61	0.96	0.92	1.06	0.47	31.47	31.76	36.77
	PMD010	0.49	0.97	0.58	0.59	0.40	0.49	0.14	0.14	0.28	7.11	0.14	0.61	0.87	0.98	0.90	0.37	28.98	32.87	38.14

Note: 1: Ts/(Ts + Tm); 2: Ts/Tm; 3: C₃₁22S/(22S + 22R); 4: C₃₂αβ22S/(22S + 22R); 5: C₂₉ααα20S/(20S + 20R); 6: C₂₉αββ/(ααα + αββ); 7: βα-moretane/αβ-hopance; 8: Gammacerane/αβ-hopance; 9: 4-Methyl sterane/Regular sterane; 10: C₃₀αβ-hopance/C₂₉Sterane; 11: Gammacerane/C₃₀-hopance; 12: Gammacerane/0.5C₃₁αβ(22R + 22S); 13: C₂₁/C₂₃tricyclic terpane; 14: C₂₆/C₂₅tricyclic terpane; 15: (Pregnane + homopregnane)/C₂₇ regular sterane; 16: Regular sterane/Hopance; 17: Regular steranes.

4.6. Steroid

According to the M/z217 mass fragmentograms of saturated hydrocarbon fractions, steroid is dominated by C₂₇–C₂₉ regular sterane (Figure 7). The content of pregnane and homopregnane are relatively high with some rearranged sterane abundance. The $\alpha\alpha\alpha$ 20R regular sterane is dominated by C₂₇, C₂₈, and C₂₉, showing the “V” distribution shape and high C₂₇ abundance (Figure 7).

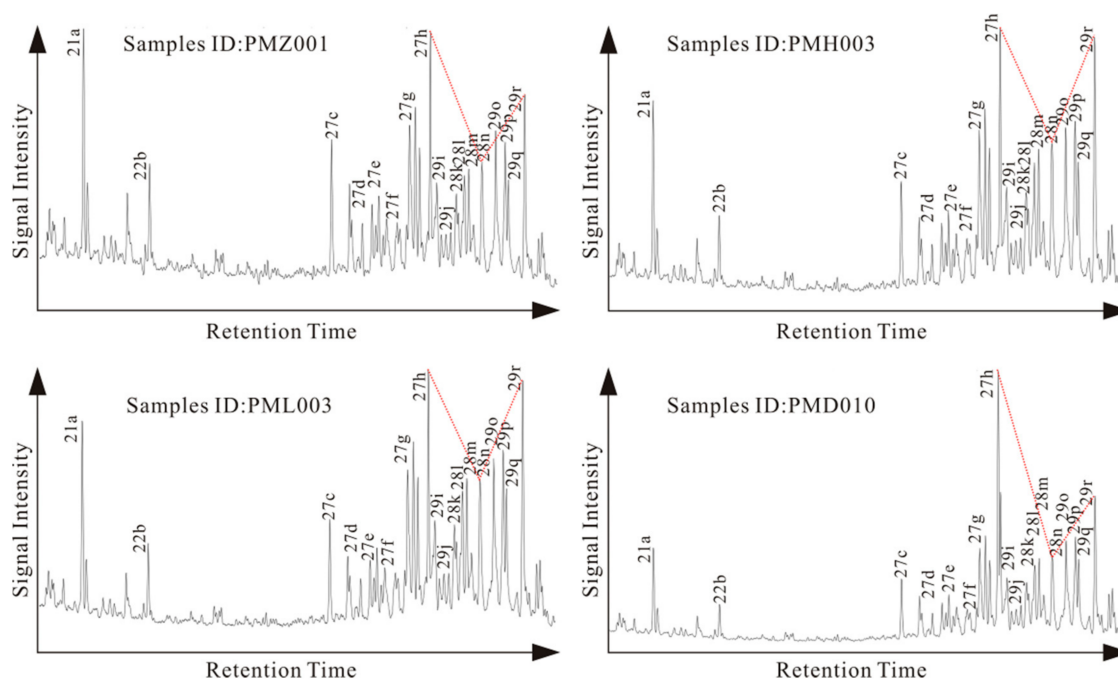


Figure 7. M/z217 mass fragment grams of saturated hydrocarbon fractions.

The (Pregnane + homopregnane)/C₂₇ regular sterane of Niutitang Formation is 1.45 and 0.95, with 0.40 and 1.00 of regular sterane/hopane (Table 5). The (Pregnane + homopregnane)/C₂₇ regular sterane of Longmaxi Formation is 1.06 and 0.90, with 0.47 and 0.37 of regular sterane/hopane (Table 5). The abundance of pregnane and homopregnane can reflect the degree of biodegradation, and the high content of them also indicates that the samples underwent strong biodegradation.

5. Discussion

5.1. Organic Matter Characteristic

5.1.1. Organic Matter Abundance

Directly associated with paleoproductivity and producing hydrocarbons content, organic matter abundance is one of the most important indexes of source rock evaluation [39]. The TOC analyses results indicate that the TOC of the shale samples of Niutitang Formation and Longmaxi Formation ranges in 1.15–3.66 wt % and 3.14–4.42 wt % (Table 3). Previous studies classified 0.4–0.6, 0.6–1.0, 1.0–2.0, and >2.0 as poor, fair, good and very good when applying this standard in Paleozoic source rocks [40,41]. Therefore, the shale from Niutitang Formation is regarded as the good type and Longmaxi Formation is the very good type. Furthermore, the diagrams of TOC-S₁ + S₂ and TOC-S₂ can also illustrate organic matter abundance. In Figure 8A,B, the samples of Niutitang Formation mainly plot in good area while those of Longmaxi Formation are largely in very good areas, which shows the same recognition with TOC classification. It is noteworthy that, in Figure 8B, all the samples plot in gas prone area, probably suggesting that the source rocks of both formations have reached maturity.

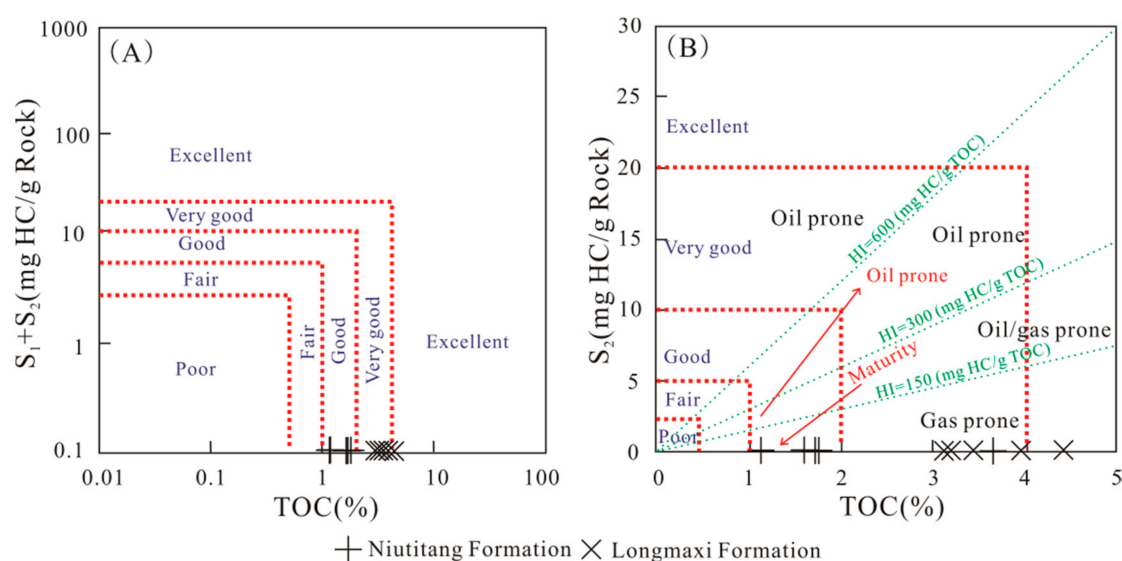


Figure 8. Cross diagrams of TOC versus S₁ + S₂ (A), and S₂ (B). (A,B) Base map is from Gao et al. [42].

5.1.2. Organic Matter Type

For Paleozoic source rocks, conventional methods such as Rock-Eval, don not work anymore [43]. Relatively accurate and efficient methods are maceral examination and organic carbon isotope [43]. In this study, maceral examination was adopted to ascertain organic matter type. From the results of maceral examination, the sapropelinite of the samples all show high abundance, while vitrinite and inertinite show less. No exinite is examined in all samples (Table 2). The Type Index (TI) can be calculated by using the equation: $TI = [A \times 100 + B \times 50 + C \times (-75) + D \times (-100)]/100$. The A, B, C, and D represent sapropelitic, exinite, vitrinite, and inertinite, respectively [39]. The TI ranges of >80, 80–40, 40–0 and <0 indicate Type I, Type II₁, Type II₂, and Type III [44]. After calculating the maceral concentration, the TI of the samples of both Niutitang Formation and Longmaxi Formation are over 80 (Table 2), implying that the organic matter types of the shale of both formations are Type I.

5.1.3. Organic Matter Maturity

The maturity of organic matter can reflect the degree of organic matter evolution. Its common indicators are T_{max}, Ro, biomarkers, etc. [45–47]. Usually, T_{max} with the range of <437, 437–450, >450 is classified as immaturity, low-maturity, and maturity [45–47]. As discussed in Section 4.3, the T_{max} of Niutitang Formation and Longmaxi Formation vary in the range of 486–511 °C and 517–580 °C (Table 3). All the T_{max} analyses show that the siliceous shale of Niutitang Formation and Longmaxi Formation has reached maturity. T_S/(T_m + T_s) ratio increases with the rising maturity and stays around 0.5 in the late hydrocarbon generation period [42,48]. The ratios of both Niutitang Formation and Longmaxi Formation samples are all 0.49 (Table 5), further implying that the shales of Niutitang Formation and Longmaxi Formation have entered maturity.

Besides, the diagrams of OEP-CPI and C₂₉steraneββ/(ββ + αα) – αααC₂₉sterane20S/(20S + 20R) also show that the samples of both Niutitang Formation and Longmaxi Formation have entered maturity and stay in the gas prone stage right now (Figure 9).

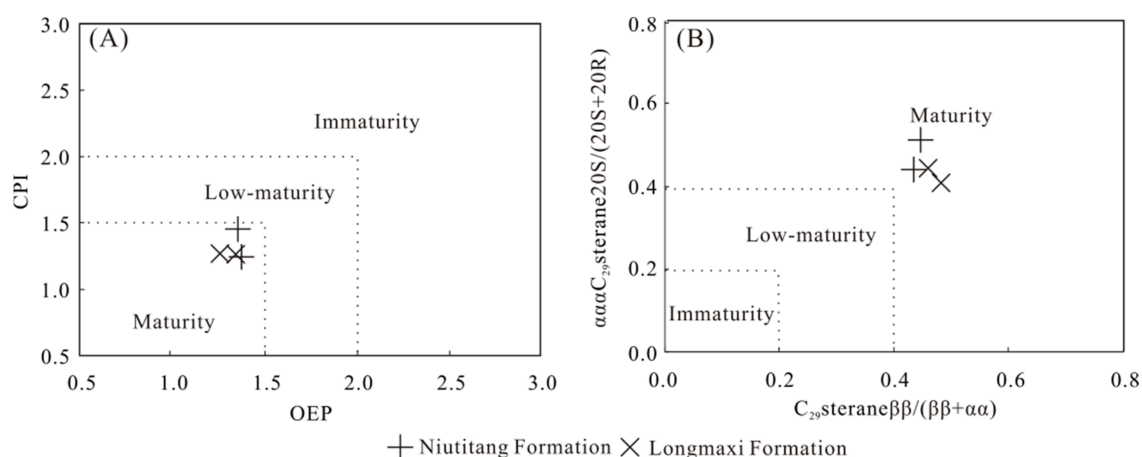


Figure 9. Cross diagrams of OEP versus CPI (A), and the $C_{29}sterane\ \beta\beta/(\beta\beta + \alpha\alpha)$ versus $\alpha\alpha\alpha C_{29}sterane\ 20S/(20S + 20R)$ (B). (A,B) Base map is from Li et al. [31].

5.2. Sedimentary Paleo-Environment

5.2.1. Organic Matter Origin

Biomarkers can provide organic matter information comprehensively, especially organic matter origin. $(nC_{21} + nC_{22})/(nC_{28} + nC_{29})$ ratio is the most common proxy to identify hydrocarbon precursor types of marine and lacustrine. The ratio ranging in 0.6–1.2 and 1.5–2.0 manifest lacustrine and marine organic matter input, respectively [35]. As can be seen from the Table 4, the ratios of both Niutitang Formation and Longmaxi Formation are all over 1.5, illustrating that organic matter stems from marine environment.

The distribution pattern of tricyclic terpane C_{21} , C_{23} and C_{24} can illustrate organic matter input, to some extent [46,48]. Researchers found that the “V” shape of C_{21} , C_{23} , and C_{24} in tricyclic terpane is usually associated with a salt-water environment and can reflect lower biological input of bacteria and algae [36]. As can be seen in Figure 6, all the samples show the obvious “V” shape of C_{21} , C_{23} , and C_{24} , suggesting the organic matter origins of Niutitang Formation and Longmaxi Formation are both bacteria and algae.

Normally, C_{27} and C_{28} regular sterane origin from lower aquatic algae, while, C_{29} regular sterane could stem from both lower aquatic algae and higher terrestrial plants [49,50]. After the source rock studies from Ediacaran and Cambrian, Zhang et al. [51] found about 20–26% C_{28} regular sterane and reckoned that C_{28} regular sterane comes from diatoms. The C_{28} regular steranes of the shale samples from Niutitang Formation and Longmaxi Formation are all over 30% (Table 3), further suggesting that the organic materials are from lower aquatic organisms and algae.

Pregnane and homopregnane are all detected in the samples of both Niutitang Formation and Longmaxi Formation. Relatively high pregnane series abundance reflect not only salinization degree of sedimentary water and biodegradation intensity, but also their affiliation of algae source [52]. The $(Pregnane + homopregnane)/C_{27}$ regular sterane of the samples of Niutitang Formation and Longmaxi Formation vary in small range with relatively low values (Table 3), showing that on the one hand, the salinity of the water is not high, on the other hand, the samples underwent biodegradation, resulting in relatively low sterane concentration.

The diagrams of C_{21}/C_{23} tricyclic terpane- C_{26}/C_{25} tricyclic terpane and Ts/Tm -Gammacerane/ C_{30} hopane also indicates that the organic matter origin of the siliceous shale of Niutitang Formation and Longmaxi Formation is aquatic organic matter in normal marine water without stratification (Figure 10).

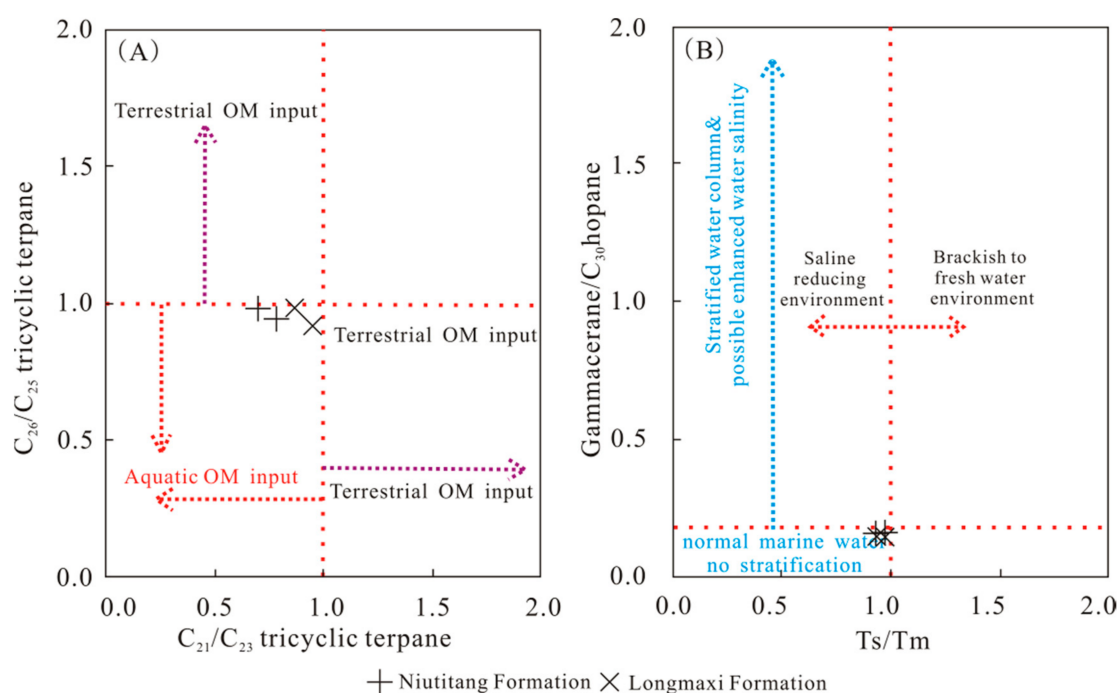


Figure 10. Cross diagrams of C_{21}/C_{23} tricyclic terpene versus C_{26}/C_{25} tricyclic terpene (A), and the Ts/Tm versus C_{30} hopane (B). (A,B) Base map is from Gao et al. [42].

5.2.2. Redox Condition

The formation mechanism of pyrite under anoxic and oxidizing environment is different and the diameter of pyrite particle can be used to distinguish the sedimentary redox condition [53]. In anoxic condition, the diameter of pyrite particle is relatively small, varying in the range of 1–18 μm with the average value of 5 μm . While in the oxidizing condition, the diameter mostly becomes bigger than 20 μm [54]. In maceral examination, a great amount of pyrite develop with solid bitumen, and pyrite framboids and pyrite mould hole can be clearly seen in both Niutitang Formation and Longmaxi Formation. The diameters of them are mostly under 1 μm (Figure 3A,D), showing that the shale of both Longmaxi Formation and Niutitang Formation deposited under anoxic condition.

Pristane (Pr) and phytane (Ph) all stem from phytol, and their abundance proportions change with the variation of redox condition [39]. In anoxic and oxidizing condition, phytol would transform to phytane and pristane, respectively. Usually, when Pr/Ph ratio is over one, it means the source rocks deposits in oxidizing condition with relatively shallow water (e.g., marsh and wetland). Especially, when the ratio is over three, it reflects the terrestrial organic matter input under weak oxidation-oxidation conditions [55]. When Pr/Ph ratio is below one, it demonstrates that the source rocks form in anoxic with relatively deep water (e.g., lacustrine fresh water lakes), and the ratio <0.6 indicates the super salt environment [56,57]. The ratios of the samples of Niutitang Formation and Longmaxi Formation are all below 1.0 (Table 4), implying that they all deposited in anoxic environment. The Pr/Ph of the sample PMZ001 is 0.58, suggesting strong salt anoxic environment.

Pr/nC_{17} and Ph/nC_{18} can well reflect the degradation of organic matter. Generally, after being affected by strong degradation, the abundance of pristane and phytane of the sample would show higher than adjacent normal alkanes [39]. The Pr/nC_{17} and Ph/nC_{18} of the samples of Niutitang Formation and Longmaxi Formation are all relatively low with a small range (Table 4), manifesting the biodegradation is not strong.

5.2.3. Salinity

Gammacerane is a kind of C_{30} triterpane, reduced from tetrahymanal [58]. Generally, gammacerane is in trace abundance in crude oil and chloroform extract [59]. However, its high abundance has closed relationship with a strong salinity environment. Therefore, gammacerane index (Gammacerane/ C_{30} -hopane) can well interpret salinity. The gammacerane index of the Longmaxi samples in northern Guizhou range from 0.97–1.35. Compared with the Cambrian source rocks (gammacerane index > 0.8) from Tarim Basin, the Longmaxi samples in northern Guizhou showing high salinity environment [51]. The gammacerane index of the shale samples in this study all show relatively low value with a small range (all below 0.2) (Table 5), reflecting their salinities are normal marine water, which is in accordance with the diagram of Ts/Tm-Gammacerane/ C_{30} hopane (Figure 10B). In addition, the gammacerane/ $0.5C_{31}\alpha\beta(22R + 22S)$ ratio can also interpret salinity. The ratios of <0.3, 0.3–0.5, and >0.5 can be regarded as fresh water, brackish water, and salt water, respectively [39]. The gammacerane/ $0.5C_{31}\alpha\beta(22R + 22S)$ of the shale samples of Niutitang Formation and Longmaxi Formation are all in the range of >0.5 (Table 5), further showing salt water environment.

6. Conclusions

The organic-rich shale of Niutitang Formation and Longmaxi Formation of Lower Paleozoic are the major source rocks in Dabashan foreland belt. The assessment results of maceral examination, TOC, and Rock-Eval show that the shale from Niutitang Formation and Longmaxi Formation are good and very good with Type I kerogen. Both of the shales have reached mature stage for generating gas. The organic matter input of organic-rich shale from Niutitang Formation and Longmaxi Formation are all derived from the lower bacteria and algae. The redox condition of them is all anoxic with no stratification and the sedimentary water is normal marine water.

Author Contributions: D.L. performed the experiments, analyzed the data and wrote the drafts of the paper, submitted the paper; R.L. conceived and designed the experiments, corrected the draft intensively; D.Z. and F.X. helped in the preparation of the paper and in checking the drafts of the paper.

Funding: This research was funded by the National Natural Science Foundation of China (No. 41173055; No. 41772118) and the Fundamental Research Funds for the Central Universities (No. 310827172101).

Conflicts of Interest: The authors declare no conflict of interest.

Appendix A

Table A1. Peak assignments for M/z191(I) and M/z217(II) mass fragmentograms of saturated hydrocarbon fractions.

Peak No.	Compound Name
(I)	
Ts	18 α (H),22,29,30-trisnorneophane
Tm	17 α (H),22,29,30-trisnorphane
29	17 α ,21 β (H)-nor-hopane
29M	17 β (H),21 α (H)-hopane(moretane)
30	17 α ,21 β (H)-hopane
30M	17 β ,21 α (H)-Moretane
31R	17 α ,21 β (H)-homohopane(22R)
32S	17 α ,21 β (H)-homohopane(22S)
32R	17 α ,21 β (H)-homohopane(22R)
33S	17 α ,21 β (H)-homohopane(22S)
33R	17 α ,21 β (H)-homohopane(22R)
34S	17 α ,21 β (H)-homohopane(22S)
34R	17 α ,21 β (H)-homohopane(22R)
35S	17 α ,21 β (H)-homohopane(22S)
35R	17 α ,21 β (H)-homohopane(22R)

Table A1. Cont.

Peak No.	Compound Name
(II)	
21a	5 α (H),14 β (H)-pregnane
22b	5 α (H),14 β (H)-homopregnane
27c	13 β (H),17 α (H)-diacholestanes 20S
27d	13 β (H),17 α (H)-diacholestanes 20R
27e	5 α (H),14 α (H),17 α (H)-cholestanes 20S
27f	5 α (H),14 β (H),17 β (H)-cholestanes 20R
27g	5 α (H),14 β (H),17 β (H)-cholestanes 20S
27h	5 α (H),14 α (H),17 α (H)-cholestanes 20R
29i	24-ethyl-13 β (H),17 α (H)-diacholestanes 20R
29j	24-ethyl-13 β (H),17 α (H)-diacholestanes 20S
28k	24-methyl-5 α (H),14 α (H),17 α (H)-cholestanes 20S
28l	24-methyl-5 α (H),14 β (H),17 β (H)-cholestanes 20R
28m	24-methyl-5 α (H),14 β (H),17 β (H)-cholestanes 20S
28n	24-methyl-5 α (H),14 α (H),17 α (H)-cholestanes 20R
29o	24-ethyl-5 α (H),14 α (H),17 α (H)-cholestanes 20S
29p	24-ethyl-5 α (H),14 β (H),17 β (H)-cholestanes 20R
29q	24-ethyl-5 α (H),14 β (H),17 β (H)-cholestanes 20S
29r	24-ethyl-5 α (H),14 α (H),17 α (H)-cholestanes 20R

References

- Wang, N.; Pei, L.; Lei, D.; Zeng, B. Analysis of unconventional gas resources distribution and development status in China. *Pet. Geol. Recovery Effic.* **2015**, *22*, 26–31. (In Chinese)
- Guo, T.; Zhang, H. Formation and enrichment mode of Jiashiba shale gas field, Sichuan basin. *Pet. Explor. Dev.* **2014**, *41*, 31–40. [[CrossRef](#)]
- Zhang, Y.; He, Z.; Jiang, S.; Lu, S.; Xiao, D.; Chen, G.; Zhao, J. Factors Affecting Shale Gas Accumulation in Overmature Shales Case Study from Lower Cambrian Shale in Western Sichuan Basin, South China. *Energy Fuels* **2018**. [[CrossRef](#)]
- Chen, F.; Lu, S.; Ding, X.; He, X. Shale gas reservoir characterization: A typical case in the Southeast Chongqing of Sichuan Basin, China. *PLoS ONE* **2018**, *13*, e199283. [[CrossRef](#)] [[PubMed](#)]
- Han, C.; Han, M.; Jiang, Z.; Han, Z.; Li, H.; Song, Z. Source analysis of quartz from the Upper Ordovician and Lower Silurian black shale and its effects on shale gas reservoir in the southern Sichuan Basin and its periphery, China. *Geol. J.* **2018**. [[CrossRef](#)]
- Li, R.; Dong, S.; Dan, L.; Duan, L. Tectonically driven organic fluid migration in the Dabashan foreland belt: Evidenced by geochemistry and geothermometry of vein-filling fibrous calcite with organic inclusions. *J. Asian Earth Sci.* **2013**, *75*, 202–212. [[CrossRef](#)]
- Li, W.; Liu, S.; Qian, T.; Dou, G.; Gao, T. Analysis of structural deformation in the north Dabashan thrust belt, south Qinling, central China. *Int. Geol. Rev.* **2014**, *56*, 1276–1294. [[CrossRef](#)]
- Wang, S.; Dai, H.; Wang, H.; Huang, Q. Source rock feature of the south of the Dabashan and Micangshan. *Nat. Gas Geosci.* **2000**, *11*, 4–16. (In Chinese)
- Jia, J.; Song, H.; Yi, H.; Chen, W. Characteristic of Paleozoic Hydrocarbon Source Rocks from Key Sections of Frontal Micangshan-Daba. *Nat. Gas Geosci.* **2011**, *22*, 1046–1053. (In Chinese)
- Li, R.; Dong, S.; Zhang, S.; Zhu, R.; Xia, B. Features and formation of organic fluids during Dabashan orogenesis. *J. Nanjing Univ. (Nat. Sci.)* **2012**, *48*, 295–307. (In Chinese)
- Hu, M.; Deng, Q.; Hu, Z. Shale gas accumulation conditions of the Lower Cambrian Niutitang Formation in Upper Yangtze region. *Oil Gas Geol.* **2014**, *35*, 272–279. (In Chinese)
- Luo, C.; Liu, S.; Sun, W.; Ran, B.; Yong, Z.; Yang, D.; Zhang, X.; Wang, S.; Ye, Y.; Deng, B. Characteristics of shale gas in the Lower Cambrian Niutitang Formation in the Upper Yangtze Region: Taking Nangao section in Danzhai as an example. *Nat. Gas Geosci.* **2014**, *25*, 453–470. (In Chinese)
- Zan, B.; Liu, S.; Ran, B.; Ye, Y.; Yang, D.; Huang, R.; Xia, G.; Jiao, K. An analysis of barite concretions from lower Silurian Longmaxi Formation on the northern margin of the Yangtze block and their genetic mechanism. *Acta Petrol. Mineral.* **2017**, *36*, 213–226. (In Chinese)

14. Xiong, G.; Wang, J.; Yu, Q.; Men, Y.; Zhou, X.; Xiong, X.; Zhou, Y.; Yang, X. Zircon U-Pb dating and geological significance of the bentonites from the Upper Ordovician Wufeng Formation and Lower Silurian Longmaxi Formation in western Daba Mountains. *Sediment. Geol. Tethyan Geol.* **2017**, *37*, 46–58. (In Chinese)
15. Lin, J.; Liu, J.; Feng, W.; Ling, X. Organic geochemical signatures and paleo-environment implications for the source rocks from the Lower Silurian Longmaxi Formation in northern Guizhou. *Sediment. Geol. Tethyan Geol.* **2014**, *34*, 79–85. (In Chinese)
16. Zhang, Y.; Li, R.; Liu, H.; Zhu, R.; Zhu, D.; Wang, N.; Zhao, B. Mesozoic-Cenozoic Tectonic Uplift History of Dabashan Foreland Structure in the Northern Rim of Sichuan Basin. *J. Earth Sci. Environ.* **2014**, *36*, 230–238. (In Chinese)
17. Li, J.; Zhang, Y.; Dong, S.; Shi, W. Structural and geochronological constraints on the Mesozoic tectonic evolution of the North Dabashan zone, South Qinling, central China. *J. Asian Earth Sci.* **2013**, *64*, 99–114. [[CrossRef](#)]
18. Li, Y.; Qu, G.; Liu, S.; Zhang, H. Structural characters and mechanism in the Micang Shan and southern Daba Shan mountains front. *Geotectonica et Metallogenia* **2008**, *32*, 285–292. (In Chinese)
19. Hu, J.; Shi, W.; Qu, H.; Chen, H.; Wu, G.; Tian, M. Mesozoic deformation of Dabashan curvilinear structural belt of Qinling orogeny. *Earth Sci. Front. (China Univ. Geosci. (Beijing) Peking Univ.)* **2009**, *16*, 49–68. (In Chinese)
20. Li, X.; Luo, Y.; Luo, T.; Zhou, M. Pre-early Cambrian black rock series in Chengkou district, Chongqing:(3) PGE geochemistry of lower-Cambrian Cherts in Bashan group. *Acta Mineral. Sin.* **2007**, *27*, 315–324. (In Chinese)
21. Zhang, T.; Lan, G.; Shen, Z.; Wang, S.; Jiang, Z. Early Cambrian reefs and banks development in southern margin of Daba Mt. and Micang Mt. *Nat. Gas Geosci.* **2005**, *16*, 710–714. (In Chinese)
22. Ling, S.; Wu, X.; Ren, Y.; Li, X.; Wang, G. Analysis of REE Geochemical Characteristics and Sedimentary Environment of the Early Cambrian Black Rock Strata in Daba Mountain. *Geol. Sci. Technol. Inf.* **2015**, *34*, 31–37. (In Chinese)
23. Wang, S.; Dai, H.; Wang, H.; Huang, Q. Characteristics of biomarkers of Marine source rocks in the southern margin of Dabashan and Micangshan. *Mar. Orig. Pet. Geol.* **2000**, *5*, 55–61. (In Chinese)
24. Qin, X.; Li, R.; Dong, S.; Liu, H. Tectonic fluid and its formation conditions of Dabashan intra-continent orogenic belt. *Earth Sci. Front.* **2016**, *23*, 183–189. (In Chinese)
25. Shi, W.; Dong, S.; Hu, J.; Zhang, Z.; Liu, G. An Analysis of Superposed Deformation and Tectonic Stress Fields of the Western Segment of Daba Mountains Foreland. *Acta Geol. Sin.* **2007**, *81*, 1314–1327. (In Chinese)
26. Cheng, W.; Yang, K. Structural evolution of Dabashan Mountain: Evidence from ESR dating. *Earth Sci. Front. (China Univ. Geosci. (Beijing) Peking Univ.)* **2009**, *16*, 197–206. (In Chinese)
27. Ye, J. *Sedimentary Facies of Lower Paleozoic in the Northern Margin of Sichuan Basin*; Northwestern University Press: Xi'an, China, 1992; pp. 55–58. (In Chinese)
28. Liu, F.; Su, C.; Yang, Y.; Li, Z.; Ye, J. Sedimentary facies analysis of Cambrian in the south of Micang Mountain. *J. Xi'an Coll. Geol.* **1987**, *9*, 3–14. (In Chinese)
29. Ye, J.; Yang, Y.; Su, C.; Li, Z.; Liu, F. An analysis of sedimentary environments of the Ordovician system in the southern slope of the Daba Mountain. *J. Xi'an Coll. Geol.* **1992**, *14*, 7–15. (In Chinese)
30. Wang, Z.; Zou, C.; Tao, S.; Li, J.; Wang, S.; Zhao, C. Analysis on tectonic evolution and exploration potential in Dabashan foreland basin. *Acta Petrolei Sin.* **2004**, *25*, 23–28. (In Chinese)
31. Li, R.; Dong, S.; Zhang, X.; Zhu, R. Formation of Natural Bitumen and its Implication for Oil/gas Prospect in Dabashan Foreland. *Acta Geol. Sin.* **2012**, *86*, 462–472.
32. Xiong, G.; Wang, J.; Li, Y.; Yu, Q.; Men, Y.; Zhou, X.; Xiong, X.; Zhou, Y.; Yang, X. Lithofacies palaeogeography of the Early Paleozoic black rock series in Dabashan region and their shale gas geological significance. *J. Palaeogeogr.* **2017**, 965–986. (In Chinese) [[CrossRef](#)]
33. Liu, J.; Zou, X.; Duan, Q.; Hu, J.; Cui, S.; Xia, J.; Gong, J. Geochemical Characteristics and Origin of the Lower Cambrian Siliceous Rocks from the Zhenping Area in North Daba Mountains. *Geol. Explor.* **2014**, *50*, 725–734. (In Chinese)
34. Yang, P.; Wang, Z.; Xie, Y.; Du, Q.; Chen, H.; He, Y. The biomarker characteristics and sedimentary environment of Lower Cambrian Niutitang Formation source rock in northern Guizhou. *Geol. Bull. China* **2012**, *31*, 1910–1921. (In Chinese)

35. Liu, W.; Lu, J. Characteristics of Organic Geochemistry of Lower Cambrian in West ern Hunan—Organic-mineralization study on MVT Lead-Zinc ore deposits. *Acta Sedimentol. Sin.* **2000**, *18*, 290–296. (In Chinese)
36. Fu, X.; Wang, J.; Wang, Z.; Chen, W. Biomarkers and sedimentary environment of Late Jurassic marine oil shale in Qiangtang basin, northern Xizang and its geological significance. *Geochimica* **2007**, *36*, 486–496. (In Chinese)
37. Aquinoneto, F.R.; Trendel, J.M.; Resde, A. Occurrence and formation of tricyclic and tetracyclic terpanes in sediments and petroleum. In Proceedings of the International Meeting on Organic Geochemistry, The Hague, The Netherlands, 12–16 September 1983; Volume 10, pp. 659–667.
38. Peters, K.E.; Moldowan, J.M.; Schoell, M.; Hemphins, W.B. Petroleum isotopic and biomarker composition related to source rock organic matter and depositional environment. *Org. Geochem.* **1986**, *10*, 17–27. [[CrossRef](#)]
39. Li, D.; Li, R.; Zhu, Z.; Wu, X.; Cheng, J.; Liu, F.; Zhao, B. Origin of organic matter and paleo-sedimentary environment reconstruction of the Triassic oil shale in Tongchuan City, southern Ordos Basin (China). *Fuel* **2017**, *208*, 223–235. [[CrossRef](#)]
40. Dai, H.; Huang, D.; Liu, X.; Yang, Y.; He, X.; Peng, H.; Tong, J. Characteristics and Evaluation of Marine Source Rock in Southwestern Shunan. *Nat. Gas Geosci.* **2008**, *19*, 503–508. (In Chinese)
41. Tan, J.; Wang, W.; Wang, Y.; Wu, X.; Zhao, W.; Wang, J.; Zhang, M. Oraminifera as ecological indicators of polluted environments. *Mar. Geol. Front.* **2011**, *27*, 23–27. (In Chinese)
42. Gao, G.; Yang, S.; Ren, J.; Zhang, W.; Xiang, B. Geochemistry and depositional conditions of carbonate-bearing lacustrine source rocks: A case study from the Early Permian Fengcheng formation in Well FN7 of the northwestern Junggar Basin. *J. Petrol. Sci. Eng.* **2017**, *162*, 407–418. [[CrossRef](#)]
43. Liang, D.; Guo, T.; Chen, J.; Bian, L.; Zhao, Z. Some Progresses on Studies of Hydrocarbon Generation and Accumulation in Marine Sedimentary Regions, Southern China (Part 2): Geochemical Characteristics of Four Suits of Regional Marine Source Rocks, South China. *Mar. Orig. Petrol. Geol.* **2009**, *14*, 1–15. (In Chinese)
44. Zhang, S.; Liang, D.; Zhang, D. Evaluation criteria for Paleozoic effective hydrocarbon source rocks. *Petrol. Explor. Devel.* **2002**, *29*, 8–12. (In Chinese)
45. Jiang, F.; Hu, T.; Liu, L.; Wang, Q.; Gao, X.; Zhang, P. Geochemical and geological characteristics of the Jurassic continental black shale in the Southwestern Depression of Tarim Basin. *Geol. J.* **2018**. [[CrossRef](#)]
46. Yandoka, B.M.S.; Wan, H.A.; Abubakar, M.B.; Adegoke, A.K.; Maigari, A.S.; Haruna, A.I.; Yaro, U.Y. Hydrocarbon potential of Early Cretaceous lacustrine sediments from Bima Formation, Yola Sub-basin, Northern Benue Trough, NE Nigeria: Insight from organic geochemistry and petrology. *J. Afr. Earth Sci.* **2016**, *129*, 153–164. [[CrossRef](#)]
47. Li, Y.; Fan, T.; Zhang, J.; Zhang, J.; Wei, X.; Hu, X.; Zeng, W.; Fu, W. Geochemical changes in the Early Cambrian interval of the Yangtze Platform, South China: Implications for hydrothermal influences and paleocean redox conditions. *J. Asian Earth Sci.* **2015**, *109*, 100–123. [[CrossRef](#)]
48. Yandoka, B.M.S.; Abubakar, M.B.; Wan, H.A.; Maigari, A.S.; Hakimi, M.H.; Adegoke, A.K.; Shirputda, J.J.; Aliyu, A.H. Sedimentology, geochemistry and paleoenvironmental reconstruction of the Cretaceous Yolde formation from Yola Sub-basin, Northern Benue Trough, NE Nigeria. *Mar. Pet. Geol.* **2015**, *67*, 663–677. [[CrossRef](#)]
49. Mackenzie, A.S.; Patience, R.L.; Maxwell, J.R.; Vandenbroucke, M.; Durand, B. Molecular parameters of maturation in the Toarcian shales, Paris Basin, France—I. Changes in the configurations of acyclic isoprenoid alkanes, steranes and triterpanes. *Geochim. Cosmochim. Acta* **1980**, *44*, 1709–1721. [[CrossRef](#)]
50. Summons, R.E.; Volkman, J.K.; Boreham, C.J. Dinosterane and other steroidal hydrocarbons of dinoflagellate origin in sediments and petroleum. *Geochim. Cosmochim. Acta* **1987**, *51*, 3075–3082. [[CrossRef](#)]
51. Zhang, S.; Moldowan, J.M.; Li, M.; Bian, L.; Zhang, B.; Wang, F.; He, Z.; Wang, D. Abnormal distribution of molecular fossils in Cambrian—Precambrian strata and their biological significance. *Sci. China* **2001**, *31*, 299–304. (In Chinese)
52. Wang, Y. *Hydrocarbon Generation and Resource Evaluation of Mesozoic and Cenozoic Strata in the North Margin of Qaidam Basin*; Science Press: Beijing, China, 2004. (In Chinese)
53. Loucks, R.G.; Ruppel, S.C. Mississippian Barnett Shale: Lithofacies and depositional setting of a deep-water shale-gas succession in the Fort Worth Basin, Texas. *AAPG Bull.* **2007**, *91*, 579–601. [[CrossRef](#)]

54. Li, D.; Li, R.; Zhu, Z.; Wu, X.; Zhao, B.; Cheng, J.; Liu, F. Rare earth elements geochemistry characteristics and their geological implications of lacustrine oil shale from Chang 7 oil layer in southern Ordos Basin, China. *Geol. J.* **2017**, *52*, 119–131. [[CrossRef](#)]
55. Tissot, B. Effects on prolific petroleum source rocks and major coal deposits caused by sea-level changes. *Nature* **1979**, *277*, 463–465. [[CrossRef](#)]
56. Peters, K.E.; Moldowan, J.M. *The Biomarker Guide: Interpreting Molecular Fossils in Petroleum and Ancient Sediments*; Prentice Hall: Englewood Cliffs, NJ, USA, 1993.
57. Fu, X.; Jian, W.; Zeng, Y.; Li, Z.; Wang, Z. Geochemical and palynological investigation of the Shengli River marine oil shale (China): Implications for paleoenvironment and paleoclimate. *Int. J. Coal Geol.* **2009**, *78*, 217–224. [[CrossRef](#)]
58. Li, D.; Li, R.; Wang, B.; Liu, Z.; Wu, X.; Liu, F.; Zhao, B.; Cheng, J.; Kang, W. Study on oil-source correlation by analyzing organic geochemistry characteristics: A case study of the Upper Triassic Yanchang Formation in the south of Ordos Basin, China. *Acta Geochim.* **2016**, *35*, 408–420. [[CrossRef](#)]
59. Lin, J.; Xie, Y.; Liu, J.; Zhao, Z.; Jing, X. The biomarkers in the source rocks from the Lower Silurian Longmaxi Formation in northern Guizhou. *Sediment. Geol. Tethyan Geol.* **2010**, *30*, 104–108. (In Chinese)



© 2018 by the authors. Licensee MDPI, Basel, Switzerland. This article is an open access article distributed under the terms and conditions of the Creative Commons Attribution (CC BY) license (<http://creativecommons.org/licenses/by/4.0/>).